RESEARCH ARTICLE

Asia-Pacific Journal of
Chemical Engineering 🏛 Curtin University WILEY

Digitalized turbulent behaviors of air and rice husk flow in a vertical suspension furnace from computational fluid dynamics simulation

Soen Steven[1,2] | Elvi Restiawaty[1,3] | Pasymi Pasymi[4] |
Imam Mardhatillah Fajri[2] | Yazid Bindar[1,2,3] (ID)

[1]Department of Chemical Engineering, Faculty of Industrial Technology, Institut Teknologi Bandung, Bandung, Indonesia

[2]Biomass Technology Workshop, Institut Teknologi Bandung, Sumedang, Indonesia

[3]Department of Bioenergy Engineering and Chemurgy, Faculty of Industrial Technology, Institut Teknologi Bandung, Sumedang, Indonesia

[4]Department of Chemical Engineering, Faculty of Industrial Technology, Universitas Bung Hatta, Padang, Indonesia

Correspondence
Yazid Bindar, Department of Bioenergy Engineering and Chemurgy, Faculty of Industrial Technology, Institut Teknologi Bandung, Sumedang, Indonesia.
Email: ybybyb@fti.itb.ac.id

Abstract

The knowledge of fluid–particle flow behavior is necessary. Unfortunately, computational fluid dynamics (CFD) studies are mostly focused on developing numerical methods in detail. Instead, the CFD studies should also subtly shift to become a tool for digitalizing fluid science to guide the practical industrial aspects. Therefore, this simulation study intends to reveal the air and rice husk flow behaviors in a vertical suspension furnace, complete with presenting digital simulation data, aiming to alleviate the escape particle amount. According to this study, the escaped particle amount was suppressed under more sphere particle, smaller particle size, and feed inlet pipe that sunk into the burner. The properties change from rice husk to ash, along with temperature escalation (as in combustion phenomena), enlarging the escaped particle amount, so the cyclone should be installed to handle it. In addition, the results of digital turbulent data from CFD simulation have succeeded in intriguing and revealing the fluid–particle flow behavior in the vertical suspension furnace. The data show a close match to the real phenomena occurring inside this furnace which reflects the standard k–ε model can conclusively predict fluid–particle flow behavior without conflicting Newton's second law of particle motion.

KEYWORDS
CFD, flow behavior, flow pattern, fluids, modeling, particles

1 | INTRODUCTION

Recently, the use of biomass attracts many researchers' attention due to its sustainability and contribution to a low carbon footprint.[1–8] Rice husk, as agricultural biomass, has high heating value (2870–4067 kcal/kg) and high volatile matter (55% to 60%), so it is attractive to be exploited as fossil fuels substitute.[9,10] The green products from rice husk are mostly obtained through combustion.[11,12] It is suitable to be implemented in a vertical suspension furnace, but it has many factors that influence

the performance, such as particle size, moisture content, sphericity, feeding technique, and furnace geometry.[13–15]

To achieve biomass combustion success, it is important to understand the fluid–particle flow behavior inside the furnace.[16] Currently, it is aided by computational fluid dynamics (CFD) which has become an extensively established, robust, and low-cost tool for examining it.[17,18] As time passes, CFD has completely changed the paradigms of fluid–particle flow which used to be full of abstractions.[19] CFD has also received growing attention for its versatility whereas equipment design has to

include an intensive cost of prototyping tests and trouble-shooting industrial equipment was also nearly impossible before this era was developed.[20–22] However, apart from the advantages offered, CFD also has some limitations that need to be paid attention to.[19,23]

It should be realized that earlier CFD studies were born due to the success euphoria to solve complex phenomena through numerical methods. Unfortunately, this causes researchers to suppose the CFD with extraordinary numerical methods in describing the fluid–particle flow phenomenon is the only important aspect.[20] The embodiment in fabricating and troubleshooting the equipment that has been designed is even somewhat ruled out because it is thought to be industrial experts' responsibility.[19] The aforementioned arguments are reinforced by the study which was carried out by Norton et al. (2007) where they stated the CFD study still struggling with several issues. Those issues are high-Reynolds turbulent modeling through numerical method improvement, time stepping in transition turbulent modeling, unstructured hybrid meshes development to be incorporated into general codes, numerical observation of near-wall criterion, and mesh refinement to achieve high convergence.[24]

Accordingly, it is necessary to encourage and ensure the CFD research direction is not just a competition for developing numerical methods.[24] The CFD studies should subtly shift to become a tool for digitalizing fluid science to guide the practical industrial aspects.[25–27] Closing the gap between simulation and as-built performance should also be an elegantly discussed topic nowadays by all academicians.[22,23,28] Several studies relate to the fluid–particle flow described that particle drag force occupies an important place in the prediction of multiphase flow characteristics.[29–31] Besides, particle sphericity is truly sensitive to the flow performance while particle reflection factor is more inferior.[32] A similar statement was affirmed that fluid–particle flow in a fluidized bed system is more affected by particle sphericity rather than the reflection coefficient.[33] The research from Fotovat et al. (2015) supplemented that particle upward–downward velocity and residence time depend on the particle sphericity.[34]

Apart from that, the existing CFD studies that reveal and serve their digital simulation data are still limited. The simulation study from Ostermeier et al. (2019) mostly served contour profiles for particle temperature, solid volume fraction, mean velocity field, and volatile mass fraction in certain areas,[16] but their study has not exhibited the digital simulation data. The CFD study for simulating biomass gasification by Gao et al. (2019) has not displayed their digital simulation data but only presented temperature contours of rice husk gasification at various particle sizes and several plots related to the cold gas efficiency improvement.[35] The review study about CFD on non-spherical biomass particles by Ullah et al. (2019) has also not yet highlighted the digital simulation data.[31] The experimental and computational study of turbulent pipe flow by Lopez-Santana (2022) mostly expressed plots related to velocity and shear stress in radial pipe position,[36] and they have not even shown the digital simulation data.

Based on the previous evidence, the studies accentuating the fluid–particle flow complete with digitalized fluid science are still scarce. The purpose of this study is then to investigate the detailed flow behaviors of air and rice husk in a vertical suspension furnace, complete with presenting digital simulation data, for reducing the escape particle amount. The influences of air supply ratio, particle sphericity, particle diameter, rice husk loading rate, burner orientation, cyclone installation, feed characteristic properties, and process temperature on escaped particle amount were inspected in perusal. Afterward, the digital turbulent data of air and particle flow were pointed out and analyzed to intrigue fluid science knowledge inside this suspension furnace. Finally, the model performance validation was also held with the assistance of Newton's second law for macroscopic particle motion mechanics.

2 | INVESTIGATION METHODOLOGY

2.1 | Geometry and simulation conditions

At first, the furnace geometry followed Figure 1a,b and the burner orientation was perpendicular to the furnace. As much as 1 tonne/h of rice husk with a particle density of 661.92 kg/m^3 was injected from the feed inlet pipe. The typical excess air requirement for rice husk combustion is in the range of 40% to 100%.[9] This study selected 80% of excess air amount, and according to the study by Steven et al. (2022), it gave to the mass ratio of air and rice husk of 10.[37] The air supply was then distributed to axial, tangential, and secondary air with ratios of 25:45:30, 25:51:24, and 25:60:15. The particle size distribution followed Rosin–Rammler model with the range of 2–8 mm and varied at averaged diameters of 1, 2.5, and 4 mm. The particle sphericity was also varied at 0.25, 0.5, and 1. The reflection coefficient between particle and wall was stated as 1.

After that, the furnace was modified as given in Figure 1c. It has inner diameter of 300 mm (previously 564 mm), burner length of 650 mm (previously 500 mm),

FIGURE 1 (a) 2D sketch of vertical suspension furnace, (b) 3D geometry of vertical suspension furnace, and (c) 3D geometry of modified suspension furnace
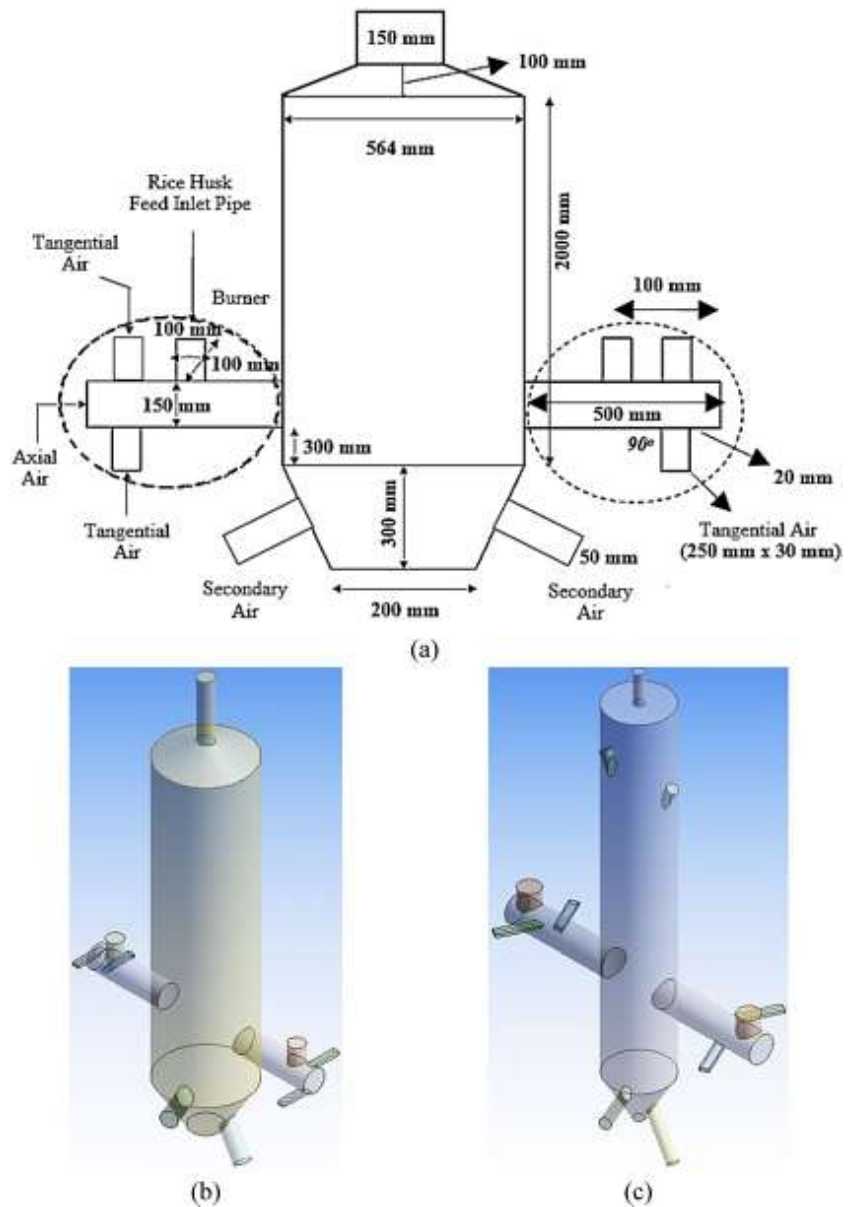
and tangential pipe angle with an angle of 45° to the burner (previously perpendicular). The angle of 45° is believed can create intense contact of air and particle in the burner with no attendance of backflow and recirculation phenomena. If the angle is between 45°–90°, the residence time of air and particle in the burner is longer, but the backflow and recirculation phenomena strongly occur. If the angle is lower than 45°, the backflow penetration depth is shorter, but the residence time of air and particle in the burner also becomes shorter.[38,39] In further, two secondary air pipes were added at the top area of the furnace (previously only at the bottom area of the furnace). Rice husk loading rates were also reduced to the values of 50, 45, 42, 41, and 40 kg/h.

The feed characteristic properties (particle density and diameter under varying mixtures of rice husk and rice husk ash) were varied at "0–100" (100% rice husk),

"25–75" (25% rice husk + 75% rice husk ash), "50–50" (50% rice husk + 50% rice husk ash), "75–25" (75% rice husk + 25% rice husk ash), and "100–0" (100% rice husk ash). The particle density of ash is 2063 kg/m³ and ash particle diameter was distributed in 0.5–1 mm with an average value of 1 mm. All mixture properties followed linear correlation. Process temperature was also varied at 25°C and 700°C. The temperature of 25°C represents the air and rice husk flow condition in absence of combustion phenomena (namely, cold flow modeling)[40] whereas the temperature of 700°C indicates the flow condition in the presence of combustion phenomena before the silica in rice husk ash transforms to crystalline phase.[14,37,41] Air density alleviates from 1.184 to 0.363 kg/m³, and air viscosity enhances from 1.84×10^{-5} to 4.09×10^{-5} Pa.s along with temperature change from 25°C to 700°C.
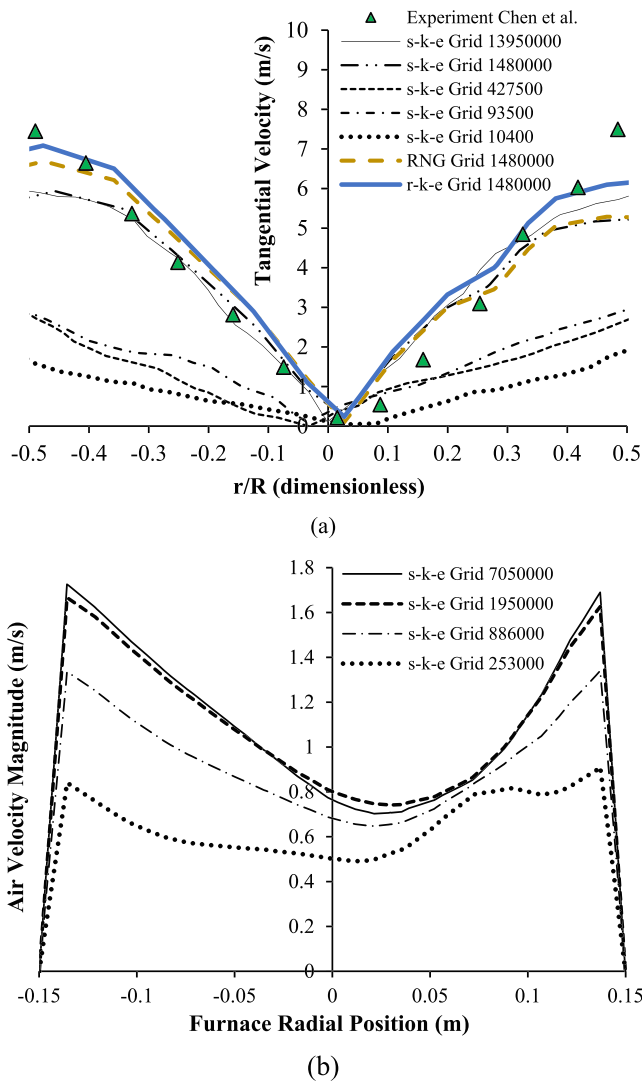
FIGURE 2 (a) Grid independence test and turbulent models validation using experiment by Chen et al. and (b) grid independence test for this study

2.2 | Governing equations

This study utilizes standard k–ε model which is widely used for fluid flow quantification in engineering problems.[18] The equations involve air density (ρ), air viscosity (μ), gravity acceleration constant (g), static pressure (p), external force (F_e), and turbulent viscosity (μ_t), as shown in Figure 2. The turbulent viscosity is then described in the forms of turbulent kinetic energy (k) and turbulent kinetic dissipation rate (ε), as served in Equation 3. The k and ε equations are given in Equations 4a and 5.

$$\frac{\partial \rho}{\partial t} + \sum_{i=x}^{y,z} \frac{\partial(\rho \overline{u_i})}{\partial i} = 0, \tag{1}$$

$$\rho \frac{\partial \overline{u_x}}{\partial t} + \sum_{i=x}^{y,z}\left[\overline{u_i}\frac{\partial(\rho\overline{u_x})}{\partial i}\right] = -\frac{\partial \overline{p}}{\partial x}$$
$$+ \sum_{i=x}^{y,z}\left\{\frac{\partial}{\partial i}\left[(\mu+\mu_t)\frac{\partial(\rho\overline{u_x})}{\partial i}\right]\right\}$$
$$+ \rho g_x + F_{e,x}, \tag{2a}$$

$$\rho \frac{\partial \overline{u_y}}{\partial t} + \sum_{i=x}^{y,z}\left[\overline{u_i}\frac{\partial(\rho\overline{u_y})}{\partial i}\right] = -\frac{\partial \overline{p}}{\partial y}$$
$$+ \sum_{i=x}^{y,z}\left\{\frac{\partial}{\partial i}\left[(\mu+\mu_t)\frac{\partial(\rho\overline{u_y})}{\partial i}\right]\right\}$$
$$+ \rho g_y + F_{e,y}, \tag{2b}$$

$$\rho \frac{\partial \overline{u_z}}{\partial t} + \sum_{i=x}^{y,z}\left[\overline{u_i}\frac{\partial(\rho\overline{u_z})}{\partial i}\right] = -\frac{\partial \overline{p}}{\partial z}$$
$$+ \sum_{i=x}^{y,z}\left\{\frac{\partial}{\partial i}\left[(\mu+\mu_t)\frac{\partial(\rho\overline{u_z})}{\partial i}\right]\right\}$$
$$+ \rho g_z + F_{e,z}, \tag{2c}$$

$$\mu_t = 0.09\rho\frac{k^2}{\varepsilon} \tag{3}$$

$$\rho\frac{\partial k}{\partial t} + \sum_{i=x}^{y,z}\left[\overline{u_i}\frac{\partial(\rho k)}{\partial i}\right] = \sum_{i=x}^{y,z}\left\{\frac{\partial}{\partial i}\left[\left(\mu+\frac{\mu_t}{1.0}\right)\frac{\partial k}{\partial i}\right]\right\}$$
$$+ G_k - Y_k, \tag{4a}$$

$$G_k = 2\mu_t\sum_{i=x}^{y,z}\left[\left(\frac{\partial\overline{u_i}}{\partial i}\right)^2\right]$$
$$+ \mu_t\sum_{i=x}^{y,z}\sum_{j=y}^{z,x}\left[\left(\frac{\partial\overline{u_i}}{\partial j}+\frac{\partial\overline{u_j}}{\partial i}\right)^2\right], \tag{4b}$$

$$Y_k = \rho\varepsilon, \tag{4c}$$

$$\rho\frac{\partial\varepsilon}{\partial t} + \sum_{i=x}^{y,z}\left[\overline{u_i}\frac{\partial(\rho\varepsilon)}{\partial i}\right] = \sum_{i=x}^{y,z}\left\{\frac{\partial}{\partial i}\left[\left(\mu+\frac{\mu_t}{1.3}\right)\frac{\partial\varepsilon}{\partial i}\right]\right\}$$
$$+ 1.44\frac{\varepsilon}{k}G_k - 1.92\rho\frac{\varepsilon^2}{k}. \tag{5}$$

Meanwhile, the particle flow is quantified by a discrete phase model which utilizes Langrangian approach.[42] According to this approach, the particle flow is only affected by the momentum balance of each particle through a particle–fluid drag coefficient (C_D).[43] This coefficient depends on sphericity (φ_p) and particle Reynolds number (Re_p) as written in Equation 6a.[44] For every particle that has density ρ_p and diameter d_p, the particle velocity field has components of $\overline{u_{px}}$, $\overline{u_{py}}$, and $\overline{u_{pz}}$. The

particle momentum conservation is then consists of drag force, gravitational force, and external force in a sequential order, as expressed in Equation 7.

$$C_D = \frac{\beta_1 Re_{p,i}}{\beta_2 + Re_{p,i}} + \frac{24}{Re_{p,i}}\left(1 + \beta_3 Re_{p,i}^{\beta_4}\right), \quad (6a)$$

$$Re_{p,i} = \frac{\rho d_p \left(\overline{u_i} - \overline{u_{pi}}\right)}{\mu}, \quad (6b)$$

$$\beta_1 = \exp\left(4.905 - 13.894\varphi_p + 18.422\varphi_p^2 - 10.260\varphi_p^3\right),$$
$$\beta_2 = \exp\left(1.468 + 12.258\varphi_p - 20.732\varphi_p^2 + 15.885\varphi_p^3\right),$$
$$\beta_3 = \exp\left(2.329 - 6.458\varphi_p + 2.449\varphi_p^2\right),$$
$$\beta_4 = 0.096 + 0.556\varphi_p, \quad (6c)$$

$$\frac{\partial \overline{u_{pi}}}{\partial t} = \left(\overline{u_i} - \overline{u_{pi}}\right)\left(\frac{3\mu C_D Re_{p,i}}{4\rho_p d_p^2}\right) + \frac{\rho_p - \rho}{\rho_p}g_i$$
$$+ F_{e,i}, \quad (i = x, y, z). \quad (7)$$

2.3 | Solution settings

The disclosed problem was solved numerically using the commercial CFD software package, ANSYS Fluent 2021 R2. The software for generating mesh used ANSYS Meshing which has already been embedded in the software itself. The tetrahedral grid size was set at 6, 9, 12, and 18 mm to generate grid numbers of 7050000, 1950000, 886000, and 253000, respectively. The standard wall function was applied and the numerical method schemes followed Table 1. The residual absolute criteria for all variables was 10^{-6} to ensure convergence. The pseudo-transient calculation with automatic time-step method and time scale factor 1 were employed for 1000 iterations.

3 | RESULTS AND DISCUSSION

3.1 | Model validation and grid independence test result

The model was first validated with the experiment by Chen et al. (1999).[45] Under standard k–ε model and grid numbers of 10400, 93500, and 427500, the resulting profiles still give a far discrepancy from the experimental data. Contrary, the grid numbers of 1480000 and 13950000 provide a meaningless difference compared to

TABLE 1 Numerical method schemes

Parameter	Value
Statement mode	Steady state
Solver	Pressure based
Pressure–velocity coupling	Coupled

Spatial discretization	Gradient: Least square cell based
	Pressure: Second order
	Momentum: Second-order upwind
	Turbulent kinetic energy:
	  First-order upwind
	Turbulent kinetic dissipation rate:
	  First-order upwind

Explicit relaxation factors	Pressure: 0.5 Momentum: 0.5 Density: 1 Body forces: 1 Turbulent kinetic energy: 0.75 Turbulent kinetic dissipation rate: 0.75 Turbulent viscosity: 1

the experimental data, as notified in Figure 2a. Despite the more accurate results being obtained under the finer grid size, it will impact greater computation time and more extravagant memory consumption.[46–48]

The grid number of 1480000 is then chosen for simulation using standard k–ε, RNG k–ε, and realizable k–ε models. The results imply that all models have tolerable precision and are close to the experiment data as long as the inspected area is not near the wall, as also plotted in Figure 2a. This is proven true because the k–ε models have a good performance in predicting swirl and fully turbulent conditions away from the wall area.[21,49,50]

Subsequently, the grid independence test is applied to the suspension furnace used in this study. It employs standard k–ε model and is performed in the radial position of the furnace chamber at a height of 1.3 m. Figure 2b informs that 1950000 is the optimal grid number to be selected because the resulting profile has not significantly changed compared to the grid number of 7050000. Ultimately, this study chooses standard k–ε model with a grid number of 1950000 due to the good agreement results and its mild demanding computation.[21,50]

3.2 | Influences of air supply ratio, particle sphericity, and particle diameter on escaped particle amount

From the macroscopic point of view, the forces that act on the particle ($\sum F$) due to fluid flow field are particle

drag force, Froude–Krylov force, mass inertia force, buoyant force, Basset force, and gravitational force. The Froude–Krylov force dominantly appears on the pressure field of the uneven flow as in ocean wave flow. Additionally, mass inertia force arises when there is an unsteady acceleration of the particle flow in a fluid flow field. The Basset force has a significant contribution to a viscous effect and the value becomes greater under large acceleration.[42,51,52]

This study dwells with air–particle fluid dynamics without fluid acceleration and is presumed to have an evenly distributed pressure field flow so that the Froude–Krylov and Basset forces can be neglected. Hence, the remaining forces that act on the particle are gravitational force (F_g), buoyant force (F_a), particle drag force (F_s), and mass inertia force (F_i). Newton's macroscopic particle flow equation is mathematically written in Equation 8a.[42,52,53] The settling velocity for single particle ($u_{t,s}$) is then calculated from Equation 8b in absence of $\frac{du}{dt}$ term. The settling velocity for particle systems (u_t) is determined from $u_{t,s}$ which is corrected by particle bed void fraction (ε, usually 0.5) and Maude–Whitmore parameter (β) as shown in Equation 9.[53,54] The laminar regime for particle flow occurs when the $Re_p < 1$ and follows Stokes' settling regime, while the turbulent regime flow occurs when $Re_p > 1000$ and follows Newton's settling regime.[53]

$$\sum F = F_g - F_a - F_s - F_i, \qquad (8a)$$

$$\frac{\pi \rho_p d_p^3}{6}\frac{du}{dt} = \frac{\pi \rho_p d_p^3}{6}g - \frac{\pi \rho d_p^3}{6\rho_p}g - \frac{C_D u_{t,s}^2 \rho A_p}{2} - \frac{\pi \rho d_p^3}{12}\frac{du}{dt}, \qquad (8b)$$

$$u_t = u_{t,s}.\varepsilon^\beta = \varepsilon^\beta.\sqrt{\frac{4d_p\left(\rho_p - \rho\right)g}{3C_D\rho\left(5.31 - 4.83\varphi_p\right)}}. \qquad (9)$$

The particle settling velocity is used to describe the escaped particle amount. The sphere particle under the air supply ratio of 25:45:30 gives the escaped particle amount of 59.79%. The Re_p for this variation is 1512.87 or in Newton's settling regime with a constant drag coefficient (C_D) in the range of 0.40–0.44.[53,55] Decreasing the secondary air ratio from 30% to 23.75% reduces the escaped particle amount from 59.79% to 41.50%, and then, the value goes up to 44.65% under secondary air ratio of 15%, as outlined in Table 2. It shows that lowering the secondary air ratio does not provide a clear pattern and disproves the escaped particle amount alleviation.

Table 2 also reveals that more non-sphere particle leads to the escalation of particle escaped amount from 44.65% to 56.64%. Under constant particle diameter and equal air flowrate at particle Reynolds number (Re_p) of 1512.87, the drag coefficient (C_D) for sphere particles is lower than non-sphere particles (0.4 vs. 1). The relationship between C_D and Re_p can be found in the graph plotted by Lapple and Shepherd (1940)[55] and Yow et al. (2005).[56] The lower drag coefficient of on-sphere particle impacts the more dominant settling velocity which alleviates the escaped particle amount.[57] The research

TABLE 2 Influence of air supply ratio and particle sphericity on escaped particle amount

Parameter	Value				
Axial air (%)	25	25	25	25	25
Tangential air (%)	45	51	60	60	60
Secondary air (%)	30	24	15	15	15
Particle sphericity	1	1	1	0.5	0.25
Escaped particle (%)	59.79	41.50	44.65	49.43	56.64

TABLE 3 Influence of particle diameter on escaped particle amount

Parameters	Value		
Axial air (%)	25	25	25
Tangential air (%)	45	60	60
Secondary air (%)	30	15	15
Particle sphericity	1	1	0.25
Escaped particle for d_p 2.5 mm (%)	59.79	44.65	56.64
Escaped particle for d_p 1 mm (%)	7.91	10.90	11.24
Escaped particle for d_p 4 mm (%)	19.04	16.89	19.55

TABLE 4 Influence on rice husk loading rate and tangential pipe angle on escaped particle amount

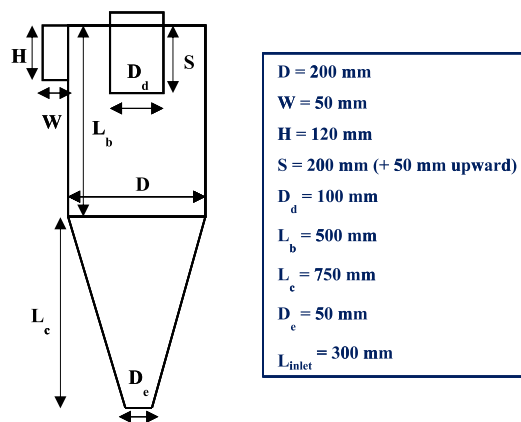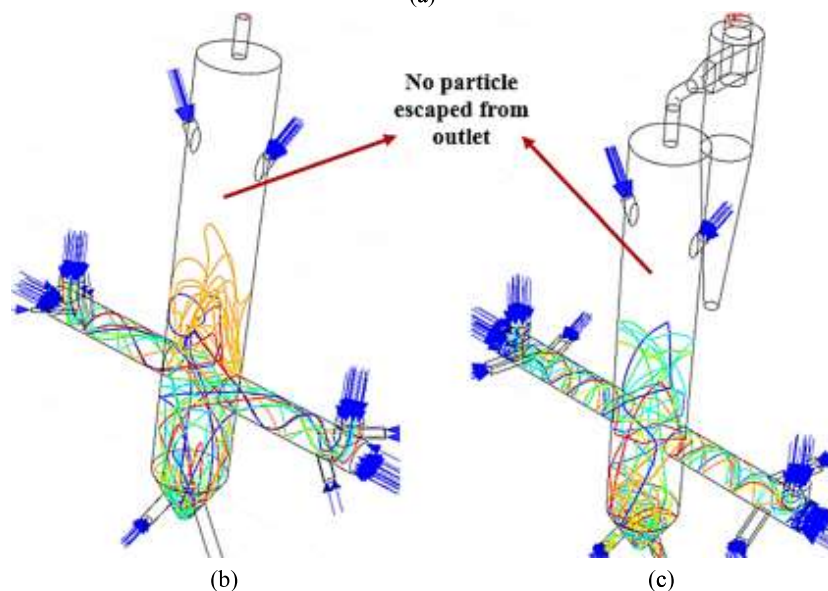| Parameters	Value			
Particle sphericity	1	1	0.5	0.25
Tangential pipe angle (°)	90	45	45	45
Escaped particle, for 50 kg/h (%)	31.15	0	7.38	9.43
Escaped particle, for 45 kg/h (%)	n.s.	0	2.15	5.12
Escaped particle, for 42 kg/h (%)	n.s.	0	1.64	1.88
Escaped particle, for 41 kg/h (%)	n.s.	0	0.75	1.02
Escaped particle, for 40 kg/h (%)	n.s.	0	0	0

Abbreviation: n.s., not simulated.

demonstrated by Dogonchi et al. (2015), as well as the review study from Hatami et al. (2017), also strengthens that a longer settling time of non-sphere particle is due to the more inferior settling velocity compared to the sphere particle.[52,58] Regarding this fact, rice husk sphericity enhancement becomes a necessity and can be fulfilled by grinding.

Interestingly, the larger particle diameter from 1 to 2.5 mm initially intensifies the escaped particle amount and then reduces under 4 mm. The Re_p for 1, 2.5, and 4 mm are 329.79, 824.47, and 1319.15, successively. It can be seen that particle diameter of 1 mm is not fully turbulent regime whereas 2.5 and 4 mm can be categorized as fully turbulent regime flow. The particle settling velocity under not fully turbulent regime has a larger value than under a turbulent regime flow.[59] Thus, it is reasonable that 1 mm of particle diameter, for all variations, gives the least escaped particle amount as tabulated in Table 3. It is also observed that large particles tended to settle, but fine material is easier to escape.[60,61]

On the other hand, the particle settling velocity in a turbulent regime flow is faster in line with a larger particle diameter.[53] This resulted in a lower escaped particle amount for particle diameter of 4 rather than 2.5 mm. Rozainee et al. (2010) also reinforce that larger size of particles was difficult to be entrained along with fluid flow.[62] Nonetheless, the smaller particle diameter has superiority in negligible internal heat and mass transport resistance which is beneficial for rice husk combustion because of more intense contact, greater degree of conversion, and swifter combustion time.[35,41] The variation of air supply ratio also does not give any pattern because the lower secondary air ratio from 30% to 15% reduces the escaped particle amount for particle diameters of 2.5 and 4 mm but not for 1 mm. Besides, the non-sphere particle ($\varphi_p = 0.25$) has a result of more escaped particle amount than sphere ($\varphi_p = 1$). Again, it is confirmed that rice husk grinding, to reduce the particle diameter and improve the particle sphericity, is important to be done.

D = 200 mm
W = 50 mm
H = 120 mm
S = 200 mm (+ 50 mm upward)
D_d = 100 mm
L_b = 500 mm
L_c = 750 mm
D_e = 50 mm
L_{inlet} = 300 mm

(a)

No particle escaped from outlet

(b)   (c)

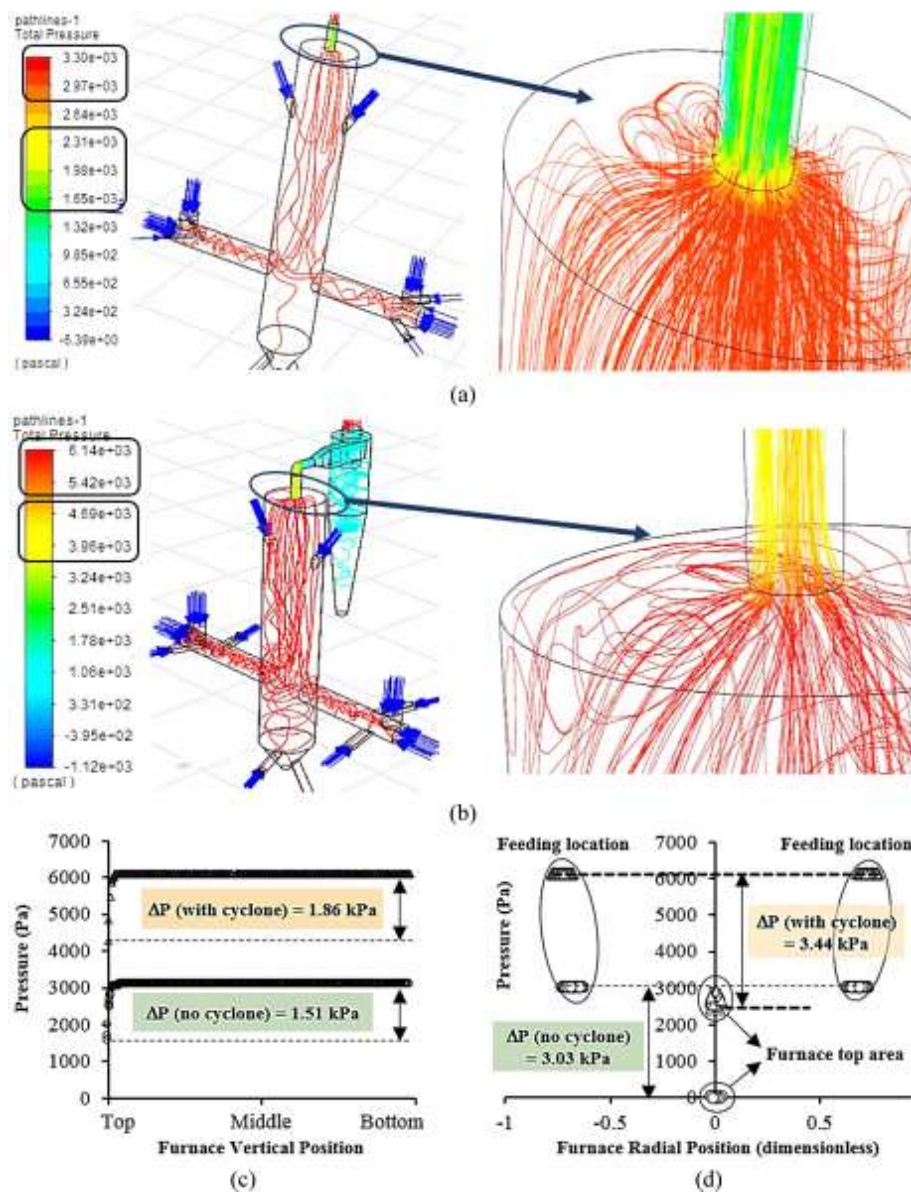**FIGURE 3** (a) Cyclone geometry, (b) particle flow behavior in the furnace without cyclone, and (c) with cyclone

3.3 | Influences of rice husk loading rate, burner orientation, and cyclone installation on escaped particle amount

The simulation was done for the furnace with a diameter of 300 mm. For rice husk loading rate of 50 kg/h and perpendicular tangential pipe orientation, the escaped particle amount is 31.15%. The value for declined rice husk loading rate and varying particle sphericity and tangential pipe orientation are given in Table 4. There is no escaped particle under rice husk loading rate of 50 kg/h and tangential pipe angle of 45° under sphere particle. Lowering the rice husk loading rate from 50 to 40 kg/h can also decrease the escaped particle amount and the rice husk loading rate of 40 kg/h gives no escaped particle for all particle sphericity values. However, the rice husk loading rate that is too low makes the operation less economic and if too high, as aforementioned, can escalate the escaped particle. Despite the more non-sphere particle going up the escaped particle, it is found that at 41 kg/h of rice husk loading rate becomes an optimal loading rate.

The cyclone separator (Figure 3a) is then installed for capturing the small amount of escaped particle.[57,60,61] After installation, in contrast, the escaped particle amount for 41 kg/h of rice husk loading rate significantly raise to 94.02% for $\varphi_p = 0.25$ and 60.85% for $\varphi_p = 0.5$, where the previous results only 1.02% and 0.75% (see Table 4). Figure 3b,c actually exhibits that rice husk particle trajectory is concentrated at the half-bottom area of the furnace. This strongly indicates that the particle are not flowing to the top area of the furnace, but a significant amount of escaped particles is caused by particles that flow out from the feed pipe location. Yet it turns out

that it is a practical common obstacle that commonly happens in rice husk continuous feeding.[63,64]

It should be noted that pressure drop definitely occurs for the flow inside cyclone.[65] This leads to the cyclone

(a)

(b)

FIGURE 5 (a) Air flow pattern in the furnace with sinking feed inlet pipe and (b) burner pressure drop for sinking and unsinking feed inlet pipe

installation creating a higher pressure drop inside the furnace. At a time, this condition can further prevent air and particle to flow into the furnace so that particles flow back to the burner and then flow out from the feeding location. It conclusively becomes the cause of the greatly increased number of recorded escaped particle amounts. Figure 4 strengthens the previous qualitative explanation where the pressure drop between the bottom and top areas of the furnace is 1.51 kPa in absence of cyclone and increases to 1.86 kPa for cyclone attendance. Also, the pressure drop between feeding location and furnace top area is 3.03 kPa for furnace without cyclone and then escalates to 3.44 kPa for furnace with cyclone.

The proposed practical solution to avoid the high amount of escaped particles from the feeding location due to cyclone installation is sinking the feed inlet pipe into burner,[63] as shown in Figure 5a. When the feed inlet pipe is sinking 3 cm into the burner, the cross-sectional area of the burner certainly narrows. Following the flow continuity principle, the axial air flow with a higher velocity and at the same time reduces the static pressure.[53] It then creates a suction effect which compels the particle to flow into the burner. Figure 5b quantitatively reinforces that pressure is higher at the feeding location area rather than inside the burner for the unsinking feed inlet pipe, making particles flow out from this area. The opposite phenomenon is found in sinking feed inlet pipe which allows the pressure inside the burner to be lower and thereby creates the suction effect.[63] Following this modification, the escaped particle amount far lessens from 94.02% to 19.00% for particle sphericity of 0.25 and from 60.85% to 11.06% for particle sphericity of 0.5.
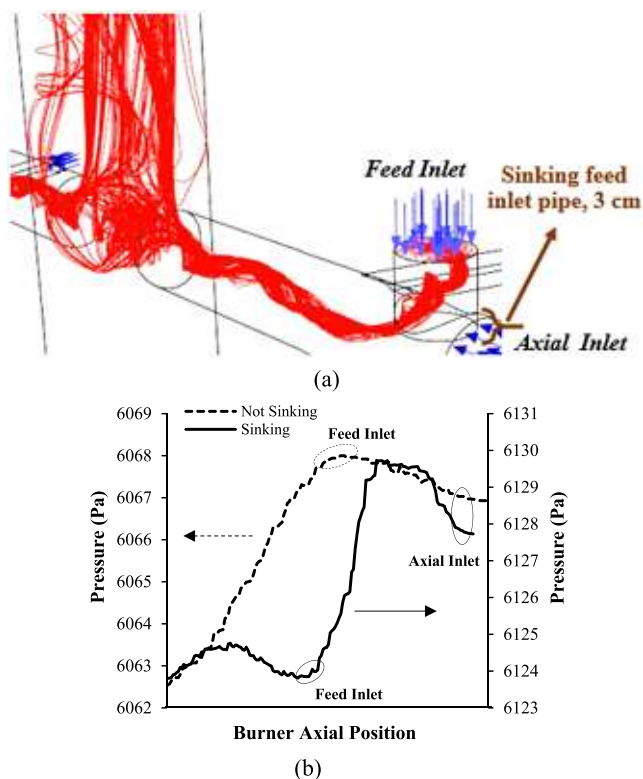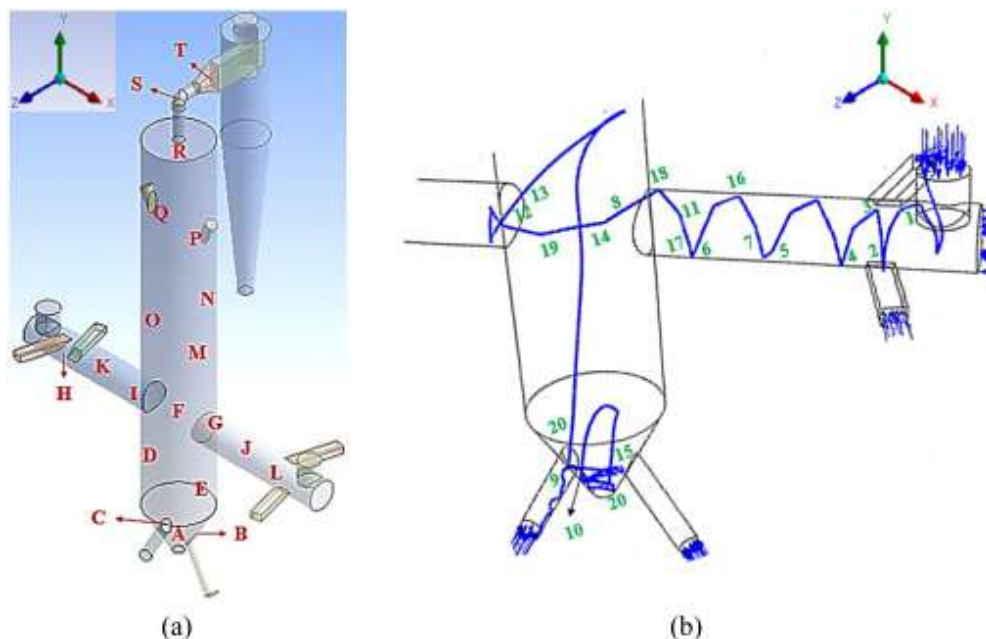

FIGURE 6 Location points to analyze digital turbulent data of (a) air flow and (b) rice husk flow

(a)

(b)

3.4 | Fluid science analysis from digital turbulent simulation data

Pointing out the digital simulation data of turbulent flow variables is no less important and actually becomes a distinct novelty in this study. The real value of the turbulent flow variables inside the vertical suspension furnace with cyclone, as well as their resulting patterns, can be examined and studied only if those data are exposed. In consequence, fluid science of it can be intrigued and scrutinized accurately and thoroughly. To achieve this goal, as many as 20 random location points inside the suspension furnace are created to analyze the digital turbulent data on air flow as depicted in Figure 6a. Subsequently, as many as 20 random location points on particle trajectory are also composed to analyze the digital turbulent data on rice husk flow (Figure 6b). Those turbulent flow variables are represented by static pressure (p), average air velocity in x-direction ($\overline{u_x}$), average air velocity in y-direction ($\overline{u_y}$), average air velocity in z-direction ($\overline{u_z}$), turbulent kinetic energy (k), turbulent kinetic dissipation rate (ε), average particle velocity in x-direction ($\overline{u_{px}}$), average particle velocity in y-direction

($\overline{u_{py}}$), average particle velocity in z-direction ($\overline{u_{pz}}$), and turbulent intensity.

The digital turbulent data for air flow are summarized in Table 5. The value of p inside the furnace seems similar except at points S and T. The highest total averaged velocity appears at point S making the lower static pressure here. The vacuum condition occurs at point T as a consequence of duct enlargement which generates eddies and internal recirculation area.[21,53] The value of $\overline{u_x}$ is found higher at points G and J as well as at points I and K in line with the axial air direction. The negative sign signifies against the axis, and the positive sign means parallel to the axis. Contrary, the largest value for $\overline{u_y}$ is nominated at point S. The value is positive because the flow direction being in line with the y-axis direction.

The flow of axial, secondary, and tangential air entirely enters the cyclone inlet, and accordingly, point T is the highest value for $\overline{u_z}$. The second-largest value for $\overline{u_z}$ is found at points H and L because they are close to the tangential air supply. Other than that, the substantial values of k, ε, and turbulent intensity are obtained in the locations that have turbulence generators or obstacles.[50,53] Hence, points H and L have significant values of

TABLE 5 Digital turbulent data of air flow at 20 location points in a vertical suspension furnace

| Location points | Coordinates | | | p (Pa) | $\overline{u_x}$ (m/s) | $\overline{u_y}$ (m/s) | $\overline{u_z}$ (m/s) | k (m²/s²) | ε (m²/s³) | Turbulent intensity (%) |
	x	y	z							
A	0	−2.4	0	6124.36	−0.041	−0.066	0.005	0.086	0.800	0.234
B	0.05	−2.37	0	6124.49	−1.111	1.735	0.233	0.044	1.007	0.165
C	−0.04	−2.37	0	6124.25	0.791	1.021	−0.383	0.118	2.978	0.269
D	−0.08	−1.98	0.04	6124.82	−0.328	0.058	−0.641	0.056	0.216	0.192
E	0.09	−2.14	−0.05	6125.18	0.302	0.199	0.537	0.059	0.301	0.194
F	0	−1.8	0	6122.96	0.228	1.948	0.023	0.543	7.491	0.602
G	0.19	−1.82	−0.05	6125.20	−3.169	3.569	−1.312	0.183	6.479	0.349
H	−0.6	−1.78	0.05	6135.94	0.983	5.618	−4.061	1.283	131.575	0.920
I	−0.2	−1.82	−0.04	6122.04	2.478	−2.897	0.828	0.222	4.365	0.384
J	0.44	−1.8	−0.04	6120.27	−2.273	3.370	0.723	0.557	14.296	0.609
K	−0.37	−1.76	0.03	6127.73	2.561	2.678	−3.431	0.299	17.812	0.446
L	0.52	−1.77	0.06	6127.88	−2.112	−3.095	4.583	0.772	58.394	0.715
M	0.02	−1.55	−0.03	6123.50	−0.022	1.137	−0.175	0.343	2.138	0.478
N	0.11	−1.11	−0.05	6123.43	−0.027	1.118	−0.650	0.243	3.529	0.369
O	−0.09	−1.31	0.06	6123.64	0.259	0.584	0.127	0.114	0.513	0.276
P	0.14	−0.88	0.03	6118.90	−0.039	−0.116	−0.130	0.713	43.149	0.663
Q	−0.12	−0.86	0.03	6119.50	−0.199	−0.266	−0.093	0.494	6.173	0.569
R	0.05	−0.53	0.03	6111.92	−2.113	2.529	−2.056	1.825	51.247	1.054
S	0	−0.35	0	2699.23	0.386	55.317	−1.136	34.945	19841.3	4.825
T	0	−0.27	−0.3	−140.24	−2.169	−2.807	−38.611	68.069	26925.1	6.735

k, ε, and turbulent intensity for they are close to the tangential air supply as turbulence generators. Point P also has quite large values of k, ε, and turbulent intensity because near to the upper secondary air supply as turbulence generators. Likewise, points R, S, and T have a high value of k, ε, and turbulent intensity due to the appearance of obstacles in terms of sudden contraction (points R and S) and sudden enlargement (point T).

It should be noticed that air fills the entire furnace's inside so it can be analyzed in any location (represented by 20 alphabets in Figure 6a). In contrast with particle flow, it does not fill the entire furnace and is only found in certain locations. Thus, the digital turbulent data for particle flow must lie in the single-particle trajectory that is released from the feed inlet pipe (reflected by 20 numbers in Figure 6b). Based on Table 6, it is agreed that a low value of average particle velocity is found at points 9, 10, 15, and 20 because they are located in the bottom area of the furnace. On the other hand, the two highest average particle velocities are at points 17 and 11 which are both near the burner ends.

The visualization of air and rice husk flow behaviors at several locations are then disclosed in terms of flow lines released from one single point. The air that flows in the burner consists of axial and tangential air in such a way that generates swirls before flowing upward and entering the cyclone unit (Figure 7a,c,d). Meanwhile, the air from the secondary pipe location directly flows to the top of the furnace (Figure 7b) or initially forms swirls at the bottom area before flowing upwards (Figure 7e). Furthermore, the particle trajectory inside the burner entirely forms an intense swirl flow as in Figure 8. This clearly proves the tangential air pipe angle of 45° is able to create perfect fluid–particle contact. The particle trajectory finally ends at the bottom of the furnace, either through direct downward flow (Figure 8a,e) or being dragged upwards first by the air and then followed by downward flow (Figure 8b–d).

3.5 | Influences of feed characteristic properties and process temperature on escaped particle amount

This section is expected to provide a preliminary fluid–particle behavior in the furnace along with the changes in feed properties and temperature as occurs in combustion. The feed characteristic properties and process

TABLE 6 Digital turbulent data of rice husk flow at 20 location points on particle trajectory in a vertical suspension furnace

| Location points	Coordinates			$\overline{u_{px}}$ (m/s)	$\overline{u_{py}}$ (m/s)	$\overline{u_{pz}}$ (m/s)
	x	y	z			
1	0.69	−1.69	−0.03	0.10	−0.56	−0.19
2	0.63	−1.79	0.06	−0.54	−2.51	0.69
3	0.59	−1.78	−0.03	−0.79	0.44	3.33
4	0.54	−1.86	0.02	−1.24	1.13	−3.65
5	0.50	−1.81	−0.05	−1.48	3.78	0.19
6	0.28	−1.78	0.05	−1.58	−3.77	1.84
7	0.42	−1.81	0.06	−1.76	−3.79	1.28
8	0.17	−1.76	−0.04	−1.74	3.66	1.86
9	−0.16	−2.60	0.00	−0.02	0.02	−0.01
10	−0.13	−2.54	−0.01	−0.29	−0.24	−0.24
11	0.22	−1.86	−0.03	−1.77	0.69	−4.26
12	−0.08	−1.73	0.00	1.40	1.36	−1.06
13	−0.07	−1.71	−0.01	1.40	1.27	−1.06
14	0.11	−1.75	0.09	−1.89	−0.31	3.87
15	0.05	−2.38	0.04	−0.46	0.43	0.30
16	0.32	−1.76	−0.03	−1.60	0.74	4.03
17	0.24	−1.87	0.02	−1.62	−3.26	−2.94
18	0.18	−1.78	−0.05	−1.73	3.72	1.85
19	−0.05	−1.70	−0.02	1.39	1.17	−1.06
20	−0.03	−2.41	0.02	−0.41	0.33	−0.48
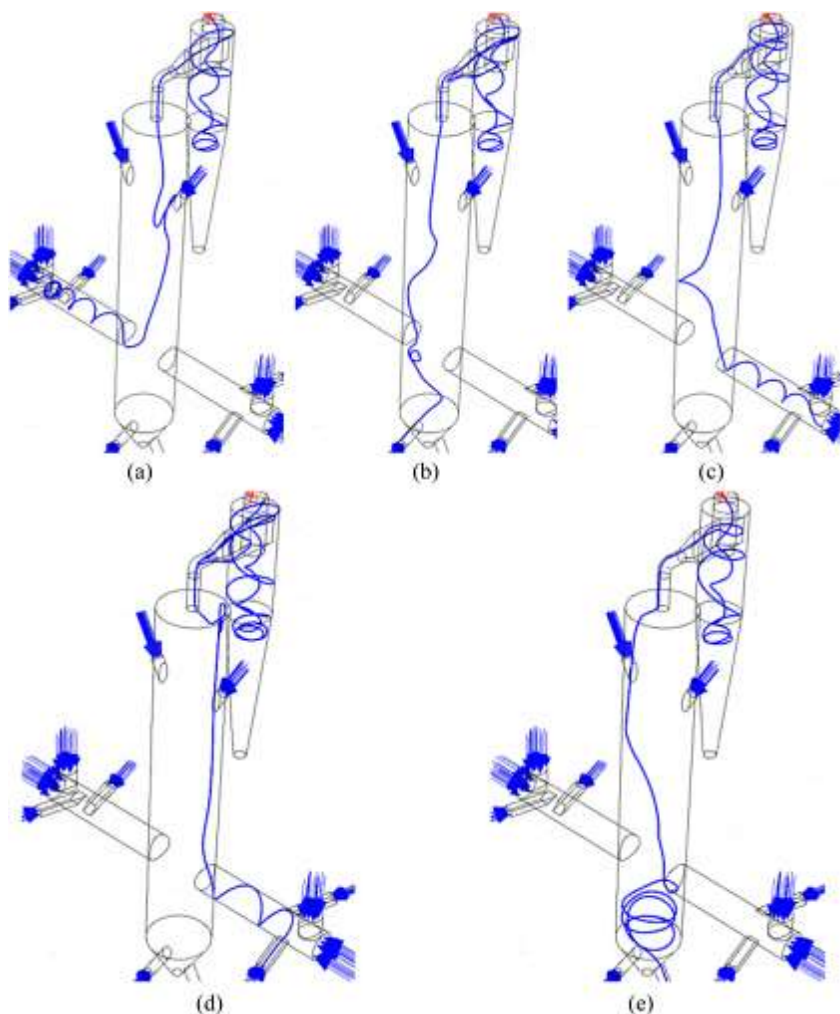
FIGURE 7 Visualization of air flow behavior (released from one single point)

temperature affect the magnitude of the forces acting on the particle and lead to the different escaped particle amounts and settling velocity. The escaped particle amount is obtained from the CFD simulation while the validation is performed using the calculation of settling velocity in Equations 8a and 9.

All variations are in the turbulent category which gives Newton's settling regime. At 25°C, the escaped particle amount is in the range of 8.70% to 17.58%, and the settling velocity is calculated in the range of 0.20–0.23 m/s whereas at 700°C increases to about 30.28% to 48.67% for escaped particle amount and 0.27–0.37 m/s for settling velocity. The escaped particle and settling velocity under various feed characteristic properties from "0–100" to "100–0" form the opposite pattern (Figure 9).

The greater composition of rice husk ash in the feed mixture augments the particle density but decreases the particle diameter. At first, the escaped particle amount weakens from "0–100" to "50–50" and the value goes up drastically from "50–50" to "100–0," both for temperatures 25°C and 700°C. This leads to the more escaped particle amount in the furnace containing rice husk ash

compared to rice husk because ash is more brittle and easier to break into smaller fragments,[66,67] making them more easily entrained.[62,64] It can be said that the lowest escaped particle amount is found at the composition of "50–50." This is supported by the calculation results from Equations 8a and 9 where the largest particle settling velocity is nominated to "50–50."

Likewise, the particle settling velocity is calculated higher at 700°C, but the escaped particle amount is also enhanced. This is because a greater drag and buoyant forces at 700°C due to lower air density and greater air viscosity occurred.[57] Consequently, the particle flow is more dominantly influenced by the drag and buoyant forces from hot air than its settling velocity due to gravity. This study finally exhibits that transformation of rice husk to ash under 700°C (as in rice husk combustion temperature) leads to smaller particle diameter, greater particle density, lower fluid density, and higher fluid viscosity. These conditions have an influence on a larger amount of escaped particles which makes cyclone installation important for combustion experiments using this furnace.[57,61]

FIGURE 8   Visualization of rice husk flow behavior (released from one single point)
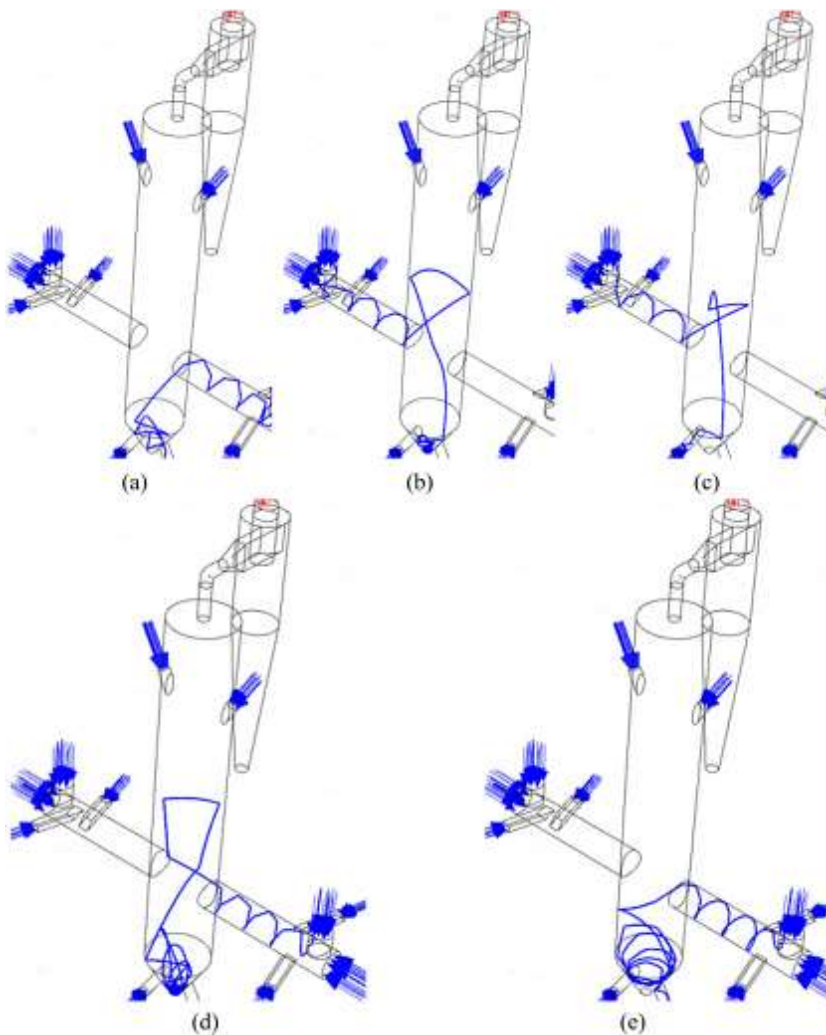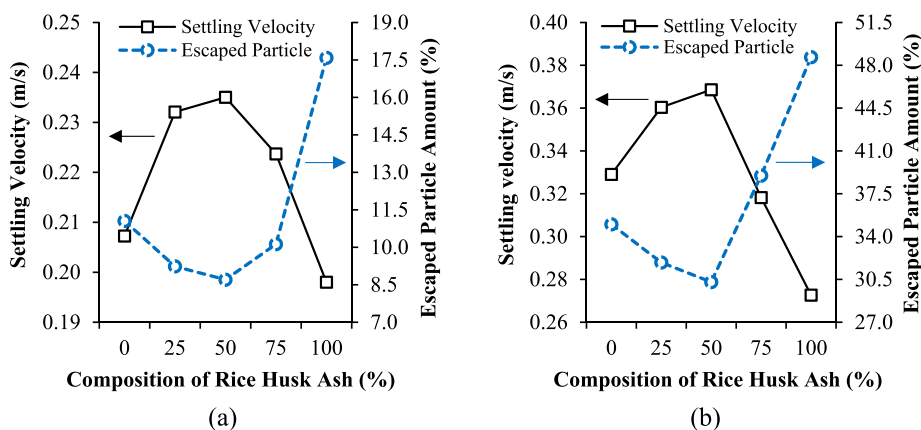

FIGURE 9   Escaped particle amount vs. settling velocity under various feed characteristics properties at (a) 25°C and (b) 700°C

Although this study has not validated the obtained simulation results with the experimental data indeed, there is some evidence that makes the results convincing. Starting from the initial validation using Chen's experiment and the results under standard k–ε model turned out to be accurate, followed by the result pattern of the escaped particle amount under several parameters which can be excellently explained by macroscopic

particle motion mechanics calculation using Newton's second law. Moreover, the digital simulation data can logically describe fluid science and detail phenomena inside the furnace. Actually, the study related to the experiment for validating fluid–particle flow behavior in the biomass cyclonic burner has been conducted by Pasymi et al. (2020) for air flow dynamics[68] and Pasymi et al. (2020) for *Mischantus* flow structure.[40] They found a close match for the flow pattern between experiment and simulation results. Therefore, the results of this simulation study imply that standard k–ε model has a robust performance to predict the fluid–particle behavior with good conformity of results to the macroscopic particle motion mechanics calculation using Newton's second law.

4 | CONCLUSIONS

The analysis of digital turbulent data from CFD simulation results has succeeded in intriguing and revealing in detail the flow behavior of air and rice husk in the vertical suspension furnace. The sphere particle with a smaller diameter decreases the escaped particle amount which leads to the necessity of rice husk grinding. The alleviation of escaped particle amount is also observed under lower rice husk loading rates and cyclone installation. Nevertheless, it precisely increases the escaped particle amount due to the larger furnace pressure drop. Interestingly, sinking the feed inlet pipe 3 cm into the burner can evidently suppress it. Furthermore, the properties change from rice husk to rice husk ash at an escalating process temperature intensifies the escaped particle, so the cyclone installation plays an important role to overcome it. Remarkably, the digital turbulent data for air and particle flow show results that can be accounted for because match the real phenomena inside the furnace. This leads to the robustness of standard k–ε model in predicting the fluid–particle flow behavior and pattern with a logical result.

ORCID

Yazid Bindar https://orcid.org/0000-0002-8075-6638

REFERENCES

1. Werther J, Saenger M, Hartge EU, Ogada T, Siagi Z. Combustion of agricultural residues. *Prog Energy Combust Sci.* 2000; 26(1):1-27. doi:10.1016/S0360-1285(99)00005-2

2. Steven S, Ramli Y, Pratama D, Restiawaty E, Bindar Y. Life cycle analysis (LCA) for silica production from three different routes: conventional, fume, and green routes. In: *International Seminar on Chemical Engineering Soehadi Reksowardojo (STKSR)*; 2020:111.

3. Budhi YW, Effendy M, Bindar Y, Subagjo S. Dynamic behavior of reverse flow reactor for lean methane combustion. *J Eng Technol Sci.* 2014;46(3):299-317. doi:10.5614/j.eng.technol.sci. 2014.46.3.5

4. Hernowo P, Steven S, Restiawaty E, et al. Chemicals component yield prediction and kinetic parameters determination of oil palm shell pyrolysis through volatile state approach and experimental study. *J Anal Appl Pyrolysis.* 2022;161:105399. doi:10.1016/j.jaap.2021.105399

5. Ramli Y, Steven S, Restiawaty E, Bindar Y. Simulation study of bamboo leaves valorization to small-scale electricity and biosilica using ASPEN PLUS. *Bioenerg Res.* 2022. doi:10.1007/s12155-022-10403-7

6. Wenten IG, Steven S, Dwiputra A, Hakim AN. From lab to full-scale ultrafiltration in microalgae harvesting. *J Phys: Conf Ser.* 2017;877(1):012002. doi:10.1088/1742-6596/877/1/012002

7. Steven S, Friatnasary DL, Wardani AK, Khoiruddin K, Suantika G, Wenten IG. High cell density submerged membrane photobioreactor (SMPBR) for microalgae cultivation. *IOP Conf Ser: Earth Environ Sci.* 2022;963(1):012034. doi:10.1088/1755-1315/963/1/012034

8. Bindar Y, Steven S, Kresno SW, et al. Large-scale pyrolysis of oil palm frond using two-box chamber pyrolyzer for cleaner biochar production. *Biomass Conv Bioref.* 2022. doi:10.1007/s13399-022-02842-1

9. Singh RI, Mohapatra SK, Gangacharyulu D. Fluidised bed combustion and gasification of rice husk and rice straw—a state of art review. *Int J Renew Energy Technol.* 2011;2(4):345-372. doi:10.1504/ijret.2011.042727

10. Wang T, Hou H, Ye Y, Rong H, Li J, Xue Y. Combustion behavior of refuse-derived fuel produced from sewage sludge and rice husk/wood sawdust using thermogravimetric and mass spectrometric analyses. *J Clean Prod.* 2019;222(2019):1-11. doi:10.1016/j.jclepro.2019.03.016

11. Quispe I, Navia R, Kahhat R. Energy potential from rice husk through direct combustion and fast pyrolysis: a review. *Waste Manag.* 2017;59:200-210. doi:10.1016/j.wasman.2016.10.001

12. Steven S, Restiawaty E, Bindar Y. Operating variables on production of high purity bio-silica from rice hull ash by extraction process. *J Eng Technol Sci.* 2022;54(3):220304. doi:10.5614/j.eng.technol.sci.2022.54.3.4

13. Blissett R, Sommerville R, Rowson N, Jones J, Laughlin B. Valorisation of rice husks using a TORBED® combustion process. *Fuel Process Technol.* 2017;159:247-255. doi:10.1016/j.fuproc.2017.01.046

14. Steven S, Restiawaty E, Bindar Y. Routes for energy and bio-silica production from rice husk: a comprehensive review and emerging prospect. *Renew Sustain Energy Rev.* 2021;149:111329. doi:10.1016/j.rser.2021.111329

15. Bindar Y. New correlations for coal and biomass pyrolysis performances with coal-biomass type number and temperature. *J Eng Technol Sci.* 2013;45(3):275-293. doi:10.5614/j.eng.technol.sci.2013.45.3.5

16. Ostermeier P, Fischer F, Fendt S, DeYoung S, Spliethoff H. Coarse-grained CFD-DEM simulation of biomass gasification in a fluidized bed reactor. *Fuel.* 2019;255(April):115790. doi:10.1016/j.fuel.2019.115790

17. Malekjani N, Jafari SM. Simulation of food drying processes by Computational Fluid Dynamics (CFD); recent advances and approaches. *Trends Food Sci Technol.* 2018;78:206-223. doi:10.1016/j.tifs.2018.06.006

18. Bindar Y. Geometry effect investigation on a conical chamber with porous media boundary condition using computational fluid dynamic (CFD) technique. *J Eng Technol Sci.* 2009;41(2):97-110. doi:10.5614/itbj.eng.sci.2009.41.2.1

19. Rojas-Sola JI, García-Baena C, Hermoso-Orzáez MJ. A review of the computational fluid-dynamics simulation software: advantages, disadvantages, and main applications. *J Magnetohydrodyn Plasma Sp Res.* 2016;23(4):417-424.

20. Khalil EE. CFD history and applications. *CFD Lett.* 2012;4(2):43-46.

21. Bindar Y. Computational engineering on multidimensional turbulent flows (Rekayasa Komputasi Aliran Turbulen Multidimensi). ITB Press; 2017.

22. Sylvia N, Mutia R, Dewi R, Bindar Y. A computational fluid dynamic comparative study on CO_2 adsorption performance using activated carbon and zeolite in a fixed bed reactor. *IOP Conf Ser: Mater Sci Eng.* 2019;536(1):012042. doi:10.1088/1757-899X/536/1/012042

23. Bindar Y. Closing the gaps between designed and operational unit process performances using CFD technique. In: *Proceeding of The Engineering Science and Technology International Conference.* Universitas Bung Hatta; 2016.

24. Norton T, Sun DW, Grant J, Fallon R, Dodd V. Applications of computational fluid dynamics (CFD) in the modelling and design of ventilation systems in the agricultural industry: a review. *Bioresour Technol.* 2007;98(12):2386-2414. doi:10.1016/j.biortech.2006.11.025

25. Ghawi AG, Kris J. Improvement performance of secondary clarifiers by a computational fluid dynamics model. *Slovak J Civ Eng.* 2011;19(4):1-11. doi:10.2478/v10189-011-0017-9

26. Nguyen N, Demirel Y. Retrofit of distillation columns in biodiesel production plants. *Energy.* 2010;35(4):1625-1632. doi:10.1016/j.energy.2009.12.009

27. Muller J, Velten K. Application of computational fluid dynamics for the optimization of homogenization processes in wine tanks. *BIO Web Conf.* 2015;5:02014. doi:10.1051/bioconf/20150502014

28. Zero Carbon Hub. Closing the gap between design and as-built performance: end of term report. 2014. https://www.zerocarbonhub.org/sites/default/files/resources/reports/Design_vs_As_Built_Performance_Gap_End_of_Term_Report_0.pdf

29. Yang S, Peng L, Liu W, et al. Simulation of hydrodynamics in gas-solid bubbling fluidized bed with louver baffles in three dimensions. *Powder Technol.* 2016;296:37-44. doi:10.1016/j.powtec.2015.09.026

30. Guan Y, Chang J, Zhang K, Wang B, Sun Q. Three-dimensional CFD simulation of hydrodynamics in an interconnected fluidized bed for chemical looping combustion. *Powder Technol.* 2014;268:316-328. doi:10.1016/j.powtec.2014.08.046

31. Ullah A, Hong K, Gao Y, Gungor A, Zaman M. An overview of Eulerian CFD modeling and simulation of non-spherical biomass particles. *Renew Energy.* 2019;141:1054-1066. doi:10.1016/j.renene.2019.04.074

32. Yin C, Rosendahl L, Kær SK, Condra TJ. Use of numerical modeling in design for co-firing biomass in wall-fired burners. *Chem Eng Sci.* 2004;59(16):3281-3292. doi:10.1016/j.ces.2004.04.036

33. Deza M, Franka NP, Heindel TJ, Battaglia F. CFD modeling and X-ray imaging of biomass in a fluidized bed. *J Fluids Eng.* 2009;131(11):111303-111313. doi:10.1115/1.4000257

34. Fotovat F, Ansart R, Hemati M, Simonin O, Chaouki J. Sand-assisted fluidization of large cylindrical and spherical biomass particles: Experiments and simulation. *Chem Eng Sci.* 2015;126:543-559. doi:10.1016/j.ces.2014.12.022

35. Gao X, Xu F, Bao F, et al. Li B Simulation and optimization of rice husk gasification using intrinsic reaction rate based CFD model. *Renew Energy.* 2019;139:611-620. doi:10.1016/j.renene.2019.02.108

36. Lopez-Santana G, Kennaugh A, Keshmiri A. Experimental techniques against RANS method in a fully developed turbulent pipe flow: evolution of experimental and computational methods for the study of turbulence. *Fluids.* 2022;7(78):1-20. doi:10.3390/fluids7020078

37. Steven S, Hernowo P, Restiawaty E, et al. Thermodynamics simulation performance of rice husk combustion with a realistic decomposition approach on the devolatilization stage. *Waste Biomass Valor.* 2022;13(5):2735-2747. doi:10.1007/s12649-021-01657-x

38. Pasymi P, Budhi YW, Bindar Y. Effects of tangential inlet shape and orientation angle on the fluid dynamics characteristics in a biomass burner. *J Phys: Conf Ser.* 2018;1090(012007):1-8. doi:10.1088/1742-6596/1090/1/012007

39. Ziqiang LV, Guangqiang L, Yingjie L. Optimization study on bias angle of a swirl burner with tangential inlet air. *Int J Smart Home.* 2016;10(3):171-180. doi:10.14257/ijsh.2016.10.3.17

40. Pasymi P, Budhi YW, Bindar Y. Intrinsic parameters of dry chopped miscanthus for cold particle dynamic modeling. *Jurnal Teknologi.* 2020;82(5):91-100. doi:10.11113/jt.v82.13534

41. Steven S, Restiawaty E, Bindar Y. Simple mass transfer simulation using a single-particle heterogeneous reaction approach in rice husk combustion and rice husk ash extraction. *IOP Conf Ser: Earth Environ Sci.* 2022;963(1):012050. doi:10.1088/1755-1315/963/1/012050

42. Corradini ML, Zhu C, Fan L-S, Jean R-H. Multiphase flow. In: *Handbook of Fluid Dynamics.* 2nd ed. Cambridge University Press; 2016:1-92. doi:10.1201/b19031-24.

43. Mandø M, Rosendahl L. On the motion of non-spherical particles at high Reynolds number. *Powder Technol.* 2010;202(1):1-13. doi:10.1016/j.powtec.2010.05.001

44. Haider A, Levenspiel O. Drag coefficient and terminal velocity of spherical and nonspherical particles. *Powder Technol.* 1989;58(1):63-70. doi:10.1016/0032-5910(89)80008-7

45. Chen J, Haynes B, Fletcher D. A numerical and experimental study of tangentially injected swirling flows. In: *2nd International Conference on CFD in the Minerals and Process Industries.* CSIRO; 1999:485-490.

46. Pasymi P, Budhi YW, Bindar Y. The effect of inlet aspect ratio (RIA) to the three dimensional mixing characteristics in tangential burner. *ARPN J Eng Appl Sci.* 2017;12(18): 5300-5306.

47. Nam H, Rodriguez-Alejandro DA, Adhikari S, Brodbeck C, Taylor S, Johnson J. Experimental investigation of hardwood air gasification in a pilot scale bubbling fluidized bed reactor and CFD simulation of jet/grid and pressure conditions. *Energy Convers Manag.* 2018;168:599-610. doi:10.1016/j.enconman.2018.05.003

48. Istadi I, Bindar Y. Improved cooler design of electric arc furnace refractory in mining industry using thermal analysis modeling and simulation. *Appl Therm Eng.* 2014;73(1): 1129-1140. doi:10.1016/j.applthermaleng.2014.08.070

49. Norton T, Tiwari B, Sun DW. Computational fluid dynamics in the design and analysis of thermal processes: A review of recent advances. *Crit Rev Food Sci Nutr.* 2013;53(3):251-275. doi:10.1080/10408398.2010.518256

50. ANSYS. ANSYS Fluent Theory Guide 2019 R3; 2019.

51. Speziale CG, So RMC. Turbulence modeling and simulation. In: *Handbook of Fluid Dynamics*. 2nd ed. CRC Press; 2016:1-64. doi:10.1201/b19031-15

52. Hatami M, Ganji DD, Sheikholeslami M. DTM for particles motion, sedimentation, and combustion. In: *Differential Transformation Method for Mechanical Engineering Problems*. Academic Press; 2017:283-336. doi:10.1016/B978-0-12-805190-0.00007-3

53. Geankoplis CJ. Principles of momentum transfer and applications. In: *Transport Processes and Unit Operations*. 3rd ed. Prentice-Hall International Inc.; 1993:114-118.

54. Maude AD, Whitmore RL. A generalized theory of sedimentation. *Br J Appl Phys.* 1958;9(12):477-482. doi:10.1088/0508-3443/9/12/304

55. Lapple CE, Shepherd CB. Calculation of particle trajectories. *Ind Eng Chem Res.* 1940;32(5):605-617. doi:10.1021/ie50365a007

56. Yow HN, Pitt MJ, Salman AD. Drag correlations for particles of regular shape. *Adv Powder Technol.* 2005;16(4):363-372. doi:10.1163/1568552054194221

57. Funk PA, Baker KD. Dust cyclone technology—a literature review. *J Cotton Sci.* 2013;17(1):40-51.

58. Dogonchi AS, Hatami M, Hosseinzadeh K, Domairry G. Nonspherical particles sedimentation in an incompressible Newtonian medium by Padé approximation. *Powder Technol.* 2015; 278:248-256. doi:10.1016/j.powtec.2015.03.036

59. Snowsill WL. Particle sizing. In: *Instrumentation Reference Book*. 4th ed. Elsevier Inc.; 2010:175-189.

60. Cortés C, Gil A. Modeling the gas and particle flow inside cyclone separators. *Prog Energy Combust Sci.* 2007;33(5): 409-452. doi:10.1016/j.pecs.2007.02.001

61. Venkatesh S, Sakthivel M, Sudhagar S, Daniel SAA. Modification of the cyclone separator geometry for improving the performance using Taguchi and CFD approach. *Part Sci Technol.* 2019;37(7):795-804. doi:10.1080/02726351.2018.1458354

62. Rozainee M, Ngo SP, Salema AA, Tan KG. Effect of feeding methods on the rice husk ash quality in a fluidised bed combustor. *Emirates J Eng Res.* 2010;15(1):1-12.

63. Pasymi P. *Innovation of Suspended Furnace Cyclone Burner for Combustion of Light Biomass Particles*. Institut Teknologi Bandung; 2019.

64. Rozainee M. *Production of Amorphous Silica From Rice Husk in Fluidised Bed System*. Universiti Teknologi Malaysia; 2007.

65. Gopani N, Bhargava A. Design of high efficiency cyclone for tiny cement industry. *Int J Environ Sci Dev.* 2011;2(5):350-354. doi:10.7763/ijesd.2011.v2.150

66. Steven S, Restiawaty E, Pasymi P, Bindar Y. An appropriate acid leaching sequence in rice husk ash extraction to enhance the produced green silica quality for sustainable industrial silica gel purpose. *J Taiwan Inst Chem Eng.* 2021;122:51-57. doi: 10.1016/j.jtice.2021.04.053

67. Steven S, Restiawaty E, Pasymi P, Bindar Y. Influences of pretreatment, extraction variables, and post treatment on bench-scale rice husk black ash (RHBA) processing to bio-silica. *Asia-Pac J Chem Eng.* 2021;16(5):e2694. doi:10.1002/apj.2694

68. Pasymi P, Budhi YW, Bindar Y. Experimental and numerical investigations of fluid flow behaviors in a biomass cyclone burner. *ASEAN J Chem Eng.* 2020;20(1):88-98. doi:10.22146/ajche.56708